ADVANCED FUNCTIONAL MATERIALS
www.afm-journal.de

Nanopore Identification of Nicotinamide Adenine Nucleotide and Its Derivatives

*Wendong Jia, Jialu Chen, Lang Yao, Panke Zhang, and Shuo Huang**

Nicotinamide adenine dinucleotide (NAD), existing primarily in two interconvertible forms: oxidized nicotinamide adenine dinucleotide (NAD^+) and reduced nicotinamide adenine dinucleotide (NADH), is an essential coenzyme in cellular energy metabolism and redox reactions. NAD related derivatives, such as oxidized nicotinamide adenine dinucleotide phosphate ($NADP^+$), reduced nicotinamide adenine dinucleotide phosphate (NADPH), nicotinic acid adenine dinucleotide (NAAD), nicotinic acid mononucleotide (NAMN), nicotinamide mononucleotide (NMN), and nicotinamide riboside (NR), are involved in the biosynthesis, metabolism, and salvage pathways of NAD^+. Their significance in cellular metabolism evaluation and disease diagnosis has led to an urgent need for the detection. Here, an engineered *Mycobacterium smegmatis* porin A (MspA) nanopore sensor, which is capable of rapidly and simultaneously identifying NAD^+ and a variety of its derivatives, is developed. With the aid of a customized machine learning algorithm, a 99.9% accuracy is achieved. Additionally, this sensor is applied to investigate the catalytic process of glucose-6-phosphate dehydrogenase (G-6-PD) by real-time monitoring of the dynamic transformations of NAD^+ to NADH and $NADP^+$ to NADPH, providing a single-molecule tool for the diagnosis of G-6-PD-related disorders.

1. Introduction

Nicotinamide adenine dinucleotide (NAD) serves as a fundamental coenzyme in cellular energy metabolism and redox homeostasis. It primarily exists in two interconvertible forms: the oxidized form NAD^+ and the reduced form NADH.[1] The dynamic equilibrium between NAD^+ and NADH is maintained through redox reactions, such as during glycolysis where NAD^+ accepts electrons and protons to form NADH, which is subsequently oxidized back to NAD^+ in the mitochondrial respiratory chain.[2] This redox cycle underpins energy transduction and metabolite transformation in biological systems.[3] The NAD^+/NADH ratio acts as a key biomarker of cellular redox status. It remains relatively stable under physiological conditions but could shift during stress or hypoxia, thereby modulating metabolic pathways and signaling cascades.[4] Quantification of NAD^+ and NADH is critical for assessing cellular metabolic phenotypes, offering valuable insights into early diagnosis and disease progression of cardiovascular and neurodegenerative diseases.[5–7]

The phosphorylation of NAD^+ by kinases generates oxidized nicotinamide adenine dinucleotide phosphate ($NADP^+$), which functions as a hydride carrier in biosynthetic processes such as photosynthesis and aberrant metabolic pathways associated with pathological states.[8] Additionally, nicotinic acid mononucleotide (NAMN) and nicotinic acid adenine dinucleotide (NAAD) represent essential intermediates in NAD^+ biosynthesis.[2,4] Analysis of these metabolites enables detailed characterization of NAD^+ synthetic capacity and identification of novel regulatory mechanisms. Meanwhile, nicotinamide mononucleotide (NMN) and nicotinamide riboside (NR) have emerged as dietary supplements capable of augmenting NAD^+ levels in vivo.[9,10] Monitoring these compounds is crucial for evaluating the efficacy and safety of nutraceutical and pharmaceutical interventions.

Numerous analytical approaches have been developed for the analysis of NAD^+ and NADH, including fluorescent probes,[11–13] genetically encoded biosensors,[14–17] and electrochemical platforms.[18–20] However, fluorescence-based methods often require intricate molecular engineering to achieve specificity, while electrochemical sensors necessitate electrode modification due to NADH's inherently high oxidation potential, leading to cumbersome fabrication processes. Notably, cross-analyte detection within the NAD^+ metabolome using these platforms remains underexplored. Liquid chromatography-tandem mass spectrometry (LC-MS/MS) has also been employed for metabolite profiling,[21] but this technique demands sophisticated sample preparation, costly instrumentation and lacks portability. Significantly, these methods typically provide ensemble-averaged results. Therefore, the development of single-molecule tools enabling simultaneous detection of NAD^+ and its derivatives is of paramount importance for unraveling complex biological processes and addressing clinical diagnostic needs.

W. Jia, J. Chen, L. Yao, P. Zhang, S. Huang
State Key Laboratory of Analytical Chemistry for Life Sciences
School of Chemistry and Chemical Engineering
Nanjing University
Nanjing 210023, China
E-mail: shuo.huang@nju.edu.cn
W. Jia, J. Chen, L. Yao, S. Huang
Chemistry and Biomedicine Innovation Center (ChemBIC)
Nanjing University
Nanjing 210023, China

The ORCID identification number(s) for the author(s) of this article can be found under https://doi.org/10.1002/adfm.202508787

DOI: 10.1002/adfm.202508787

Biological nanopores represent an emerging class of single-molecule sensors that have been extensively applied in single-molecule nucleic acid sequencing.[22] Besides sequencing, they were utilized for the sensing of amino acids,[23–25] peptides[26,27] and proteins.[28,29] They are also regarded as a promising platform for single-molecule protein sequencing in future prospects.[30] *Mycobacterium smegmatis* porin A (MspA), an octameric porin with a conical lumen geometry, demonstrates an exceptional resolution and is the first nanopore which achieved DNA sequencing.[31] When properly engineered, the MspA nanopore can be endowed with a unique reactive site and transformed into a small-molecule sensor. This sensor is capable of completely differentiating small-molecule analytes that exhibit subtle differences, such as sugars,[32,33] sugar alcohols,[34] and nucleotides.[35,36] This high resolution of this nanopore should in principle allow for the direct identification of NAD^+ and its related derivatives. Inspired by the reversible interaction between phenylboronic acid (PBA) and the ribose moiety,[37] which is a common feature in the molecular structures of NAD^+ and its related derivatives, it is hypothesized that the MspA nanopore integrated with a PBA adapter, also referred to as MspA-90PBA,[32] might be employed for the sensing of NAD^+ and its related derivatives. Although nanopore sensing of NAD^+ and NADH has been previously demonstrated using the α-hemolysin nanopore,[38] there has been no report of a nanopore that can simultaneously distinguish NAD^+ from its related derivatives.

2. Results and Discussion

2.1. Nanopore Identification of NAD^+ and NADH

Nanopore identification of NAD^+ and its derivatives was performed by MspA-90PBA. The MspA-90PBA was prepared as reported previously.[32] It contains a single PBA, intentionally designed at its constriction. Eight representative compounds, including NAD^+, NADH, $NADP^+$, NADPH, NAAD, NAMN, NMN, and NR, were selected as model compounds. These compounds all contain ribose moiety, which can reversibly bind to the PBA adapter, providing the basis of sensing.

The oxidized NAD^+ features ribose moieties capable of reversibly forming boronate esters with the PBA adapter at the pore constriction during nanopore sensing (**Figure 1a**), generating characteristic nanopore events for compound identification (Figure 1b). Nanopore measurements were initiated by spontaneous insertion of MspA-90PBA into a lipid bilayer in an electrolyte solution of 1.5 M KCl, 100 mM MOPS (pH 7.0). NAD^+ at defined concentrations were added to the *cis* chamber, and a constant +160 mV potential was applied. Immediately upon NAD^+ addition, consecutive appearance of reproducible event signatures were observed.

Notably, each NAD^+ contains two adjacent ribose groups available for PBA binding, resulting in two distinct event types with differing noise characteristics (Figure 1c,d). To systematically characterize these events, three key parameters were defined: event dwell time (t_{off}), relative current blockage ($\%I_b$) and the standard deviation of the blockage level (SD) are detailed in Figure S1 (Supporting Information). The event scatter plot of SD versus $\%I_b$ confirms the presence of two discrete event populations (Figure 1e), validated by three independent measurements (Figure S2, Supporting Information). This unambiguous resolution of binding events at different molecular sites highlights the superior discriminatory power of the MspA-90PBA.

The interconversion between NAD^+ and NADH via redox reactions constitutes a fundamental biochemical process essential for a variety of physiological functions, including cellular respiration, energy transduction, and redox homeostasis.[1] Structurally, NAD^+ features a positively charged quaternary ammonium moiety in its nicotinamide ring (Figure 1c), whereas NADH represents the reduced state with a hydride ion bound to the nicotinamide ring (Figure 1f). The subtle structural divergence between these two compounds presents technical challenges for their simultaneous discrimination in complex samples.

The above demonstrated assay was further validated for NADH sensing (Figure 1f; Figure S3, Supporting Information). Analogously to NAD^+, NADH also generated two distinct event populations characterized by unique ionic current signatures, confirmed by SD versus $\%I_b$ scatter plot results (Figure 1g,h). This behavior also arises from the presence of two adjacent ribose moieties in NADH that enable two possible configurations of PBA binding. Comparison of event distributions between NAD^+ and NADH revealed clear differences in their respective scatter plots (Figure 1e,h), demonstrating unambiguous discrimination of these structurally homologous analytes differing solely by a hydride ion. This atomic-level resolution underscores the exceptional sensing precision of MspA-90PBA as well. Control experiments using an octameric M2 MspA variant lacking the PBA conjugation yielded no measurable binding events for any above-mentioned analytes (Figure S4, Supporting Information). This result confirms that the phenylboronic acid moiety is indispensable for generating event generation.

2.2. Nanopore Identification of NAD^+ Derivatives

The analytical capabilities of MspA-90PBA were further expanded to encompass $NADP^+$, NADPH, NAMN, NAAD, NMN, and NR (**Figure 2a**). These derivatives represent key intermediates in NAD biosynthesis, redox metabolism, and salvage pathways.[2] Specifically, $NADP^+$, the phosphorylated derivative of NAD^+, serves as a hydride acceptor to form NADPH.[8] NAMN, NAAD, and NMN all act as critical NAD^+ precursors, undergoing enzymatic conversion to NAD^+ through intracellular salvage pathways that maintain cellular NAD^+ homeostasis and support essential physiological functions.[1] Notably, NMN and NR have emerged as dietary supplements capable of augmenting intracellular NAD^+ levels when co-administered.[9] Each of these compounds was independently evaluated using the MspA-90PBA.

All the measurements were identically carried out as previously demonstrated with NAD^+ and NADH. In separate measurements, each analyte was added to the *cis* chamber at the desired concentration. According to the results, all the above-mentioned compounds, except NAAD, reported a single population of nanopore events (Figure 2b–g). NAAD, which has two moieties available for PBA binding, gives rise to two characteristic binding events. The population numbers of these events were consistent with the characteristics of their molecular structures,

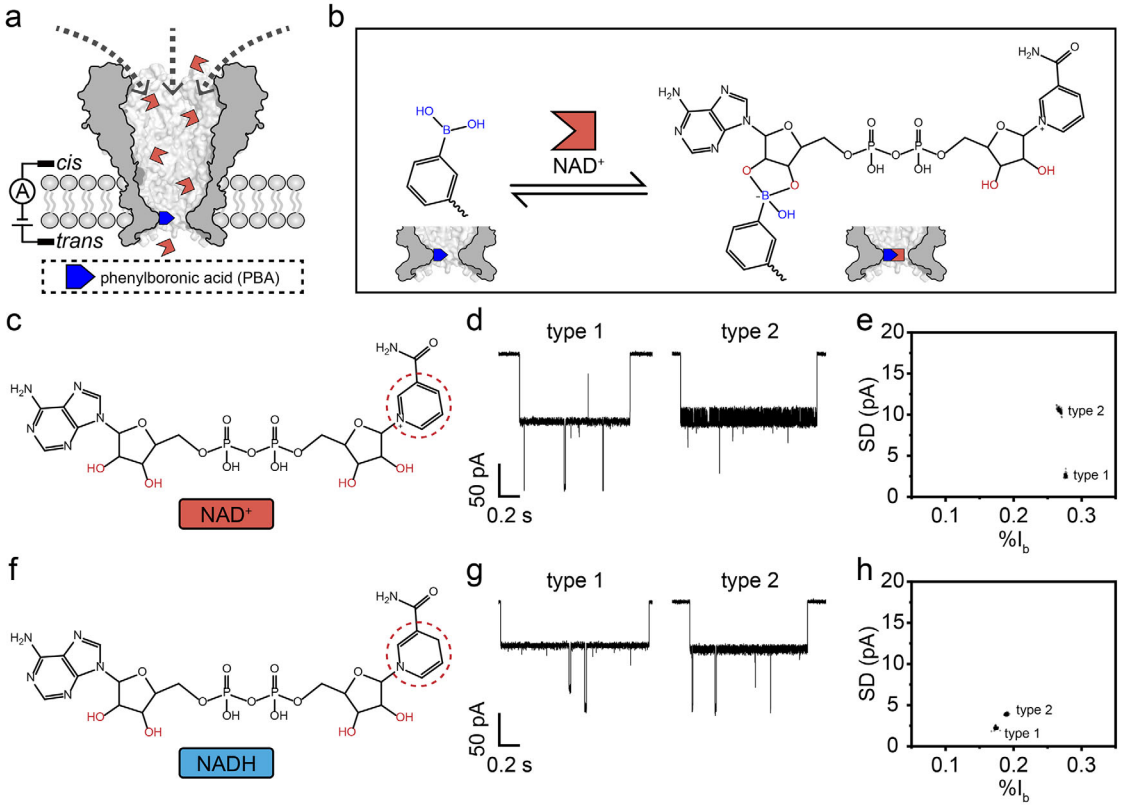

Figure 1. Nanopore identification of NAD^+ and NADH. a) The schematic diagram of NAD^+ identification performed by MspA-90PBA. The MspA-90PBA nanopore contains a single phenylboronic acid (PBA) at the pore contraction, which can form a reversible borate with the ribose of NAD^+. b) The mechanism of NAD^+ sensing. A NAD^+ molecule can reversibly bind to PBA to produce sensing events. c) The chemical structure of NAD^+. d) Representative events of NAD^+. NAD^+ contains two ribose moieties, resulting in two binding configurations and event types. e) The event scatter plot of relative current blockage ($\%I_b$) versus standard deviation (*SD*) of NAD^+ events. Two event clusters are observed in the scatter plot, respectively corresponding to two event types of NAD^+ events. f) The chemical structure of NADH. The main differences between NAD^+ and NADH are marked by the red dashed circle in c and f. g) Representative events of NADH. Two types of events were also observed, respectively corresponding to the two binding configurations of NADH and PBA. h) The event scatter plot of $\%I_b$ versus *SD* of NADH events. All measurements were performed as described in Methods. The measuring buffer was 1.5 M KCl, 100 mM MOPS, pH 7.0 and a potential of +160 mV was continually applied. NAD^+ and NADH were respectively added to the *cis* chamber with a final concentration of 1 mM. The events in the scatter plots (e, h) were extracted from a 20 min continuous trace. A total of 391 and 497 events are included in e and h, respectively.

demonstrating an interpretability for nanopore event generation. To display more sensing details, the event scatter plots and the representative traces were also shown in Figures S5–S10 (Supporting Information). Identical measurements were also carried out using the octameric M2 MspA, which lacks the PBA adapter (Figure S4, Supporting Information). As expected, no characteristic events were observed, again confirming the indispensable role of the PBA adapter in event generation.

2.3. Machine Learning Assisted Nanopore Sensing

To automatically and objectively perform event identification, a customized machine learning algorithm based on the events obtained from the previous measurements was established (Figure S11, Supporting Information). The workflow of machine learning consists of three main steps, including data collection, feature extraction, and model training. Briefly, nanopore events of NAD^+, NADH, $NADP^+$, NADPH, NAMN, NAAD, NMN, and NR were first separately collected. 1000 events acquired from each analyte were selected to form the training dataset. To ensure generality of model training, these events were derived from results of three independent measurements. Each event contains a known label, based on the analyte used for event generation. Five feature parameters, including $\%I_b$, t_{off}, *SD*, skewness (*skew*) and kurtosis (*kurt*), were extracted from each event to form the feature matrix (Table S1, Supporting Information). The feature matrix was then fed to the Classification Learner toolbox in MATLAB for model training. Various mainstream models, such as decision trees, discriminant analysis, naive Bayes, support vector machine (SVM), K-nearest neighbor (KNN) and ensemble, were used for machine learning. Ten-fold cross-validation was used to evaluate the classification accuracy of the model. Acknowledging the high resolution of MspA-90PBA, these compounds generated highly distinguishable nanopore events. Thus, all models report a high accuracy. According to the results of model training, the linear SVM model has reported the highest validation accuracy (99.9%) and the lowest total classification cost. This model was thus

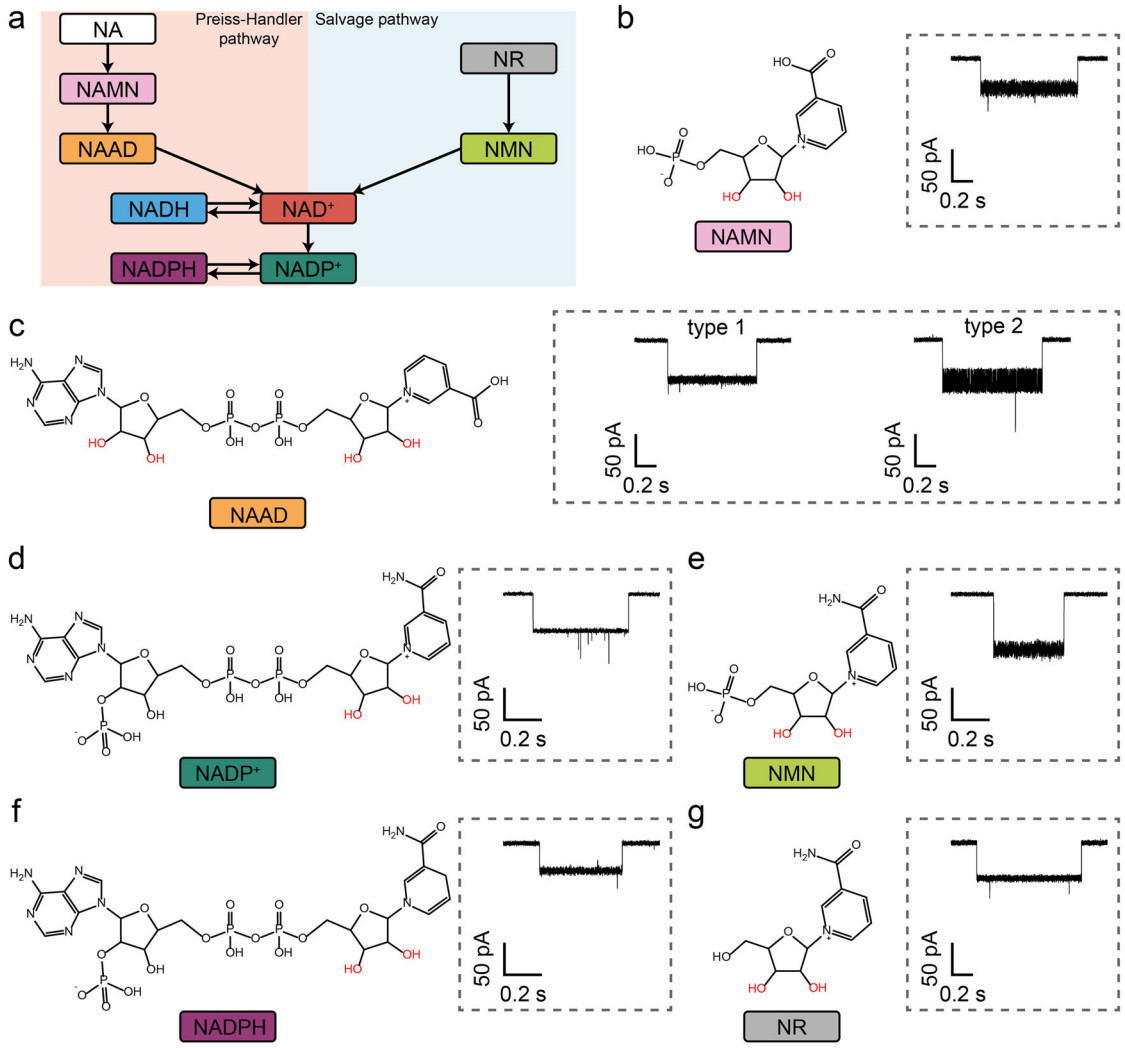

Figure 2. Identification of NAD$^+$ derivatives using MspA-90PBA. a) The synthesis, metabolism and salvage pathways of NAD$^+$. b–g) The chemical structures and representative events of NAMN (b), NAAD (c), NADP$^+$ (d), NMN (e), NADPH (f) and NR (g). Except NAAD, all compounds generated one type of event. NAAD has two binding sites compatible with PBA, leading to the generation of two types of events.

selected to perform all subsequent prediction tasks. The confusion matrix obtained based on the linear SVM model was also shown in **Figure** 3a.

The trained model was further used for the identification of unknown events obtained from simultaneous sensing of all NAD$^+$ and related derivatives in this study. Experimentally, all above-mentioned compounds were simultaneously added to the *cis* chamber during the measurements using MspA-90PBA. The event scatter plot of SD versus $\%I_b$ obtained from simultaneous sensing of these compounds was shown in Figures 3b and S12 (Supporting Information). All nanopore events were acquired from a 20 min continuous recording, and the feature parameters were extracted respectively for machine learning prediction. These nanopore events were identified by the previously trained model and color encoded according to the prediction results. A representative trace obtained from simultaneous sensing of NAD$^+$ and its derivatives was shown in Figure 3c. The event labels were identified by the machine learning model and marked on the trace. All nanopore events were clearly distinguished according to their characteristics, consistent with results obtained during separate sensing of individual compounds.

To evaluate potential interference from adenosine 5′-monophosphate (AMP) and adenosine 5′-triphosphate (ATP) in the detection of NAD$^+$ and related derivatives, nanopore events for AMP and ATP were collected under identical measurement conditions. These events were integrated with pre-existing nanopore event data to form a more comprehensive training dataset for machine learning (Figure S13, Supporting Information). Experimental results demonstrated that the trained model achieved a 99% validation accuracy in discriminating events corresponding to AMP, ATP, NAD$^+$, and its derivatives, confirming that AMP and ATP do not interfere with the detection of NAD$^+$-related analytes using this nanopore sensor. The nanopore sensor was also applied to analyze yeast extracts, enabling the identification of NAD$^+$, NADH, and NADPH components (Figure S14, Supporting Information).

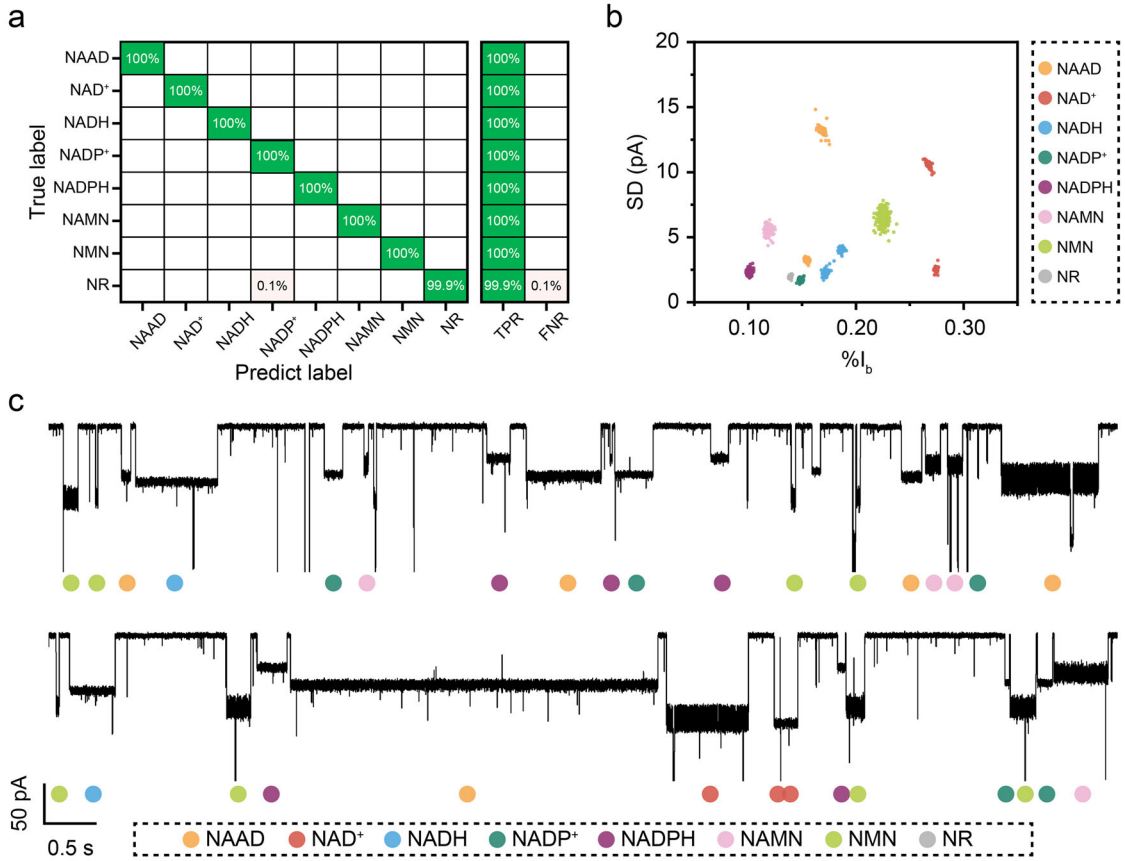

Figure 3. Machine learning assisted identification of NAD^+ and its derivatives. a) The confusion matrix generated by the linear SVM model. The true positive rate (TPR) and the false negative rate (FNR) were also demonstrated on the right. b) The event scatter plot of $\%I_b$ versus *SD* generated by simultaneous sensing of all NAD^+ and related derivatives investigated in this study. All events were identified by the previously trained model and labelled accordingly. c) A representative trace generated by simultaneous sensing of all NAD^+ and its derivatives. The events were identified by the previously trained model and marked on the traces. The measurements were performed as described in Methods. The measuring buffer was 1.5 M KCl, 100 mM MOPS, pH 7.0 and a potential of +160 mV was continually applied. Each analyte was added in *cis* chamber with desired concentrations. The events in the scatter plot were extracted from a 20 min continuous trace. A total of 2077 events are included in the scatter plot.

Additionally, significant quantities of AMP, uridine 5′-monophosphate (UMP), cytidine 5′-monophosphate (CMP), and guanosine 5′-monophosphate (GMP) were detected in the yeast extracts. These results highlight the sensor's preliminary applicability for analyzing complex biological matrices like yeast extracts.

2.4. Real-Time Monitoring of Dehydrogenase Catalysis

NAD^+ serves as the primary hydride acceptor in intracellular redox reactions across all domains of life. Its capacity to accept a hydride ion, forming its reduced counterpart NADH, is fundamental to metabolic processes such as glycolysis, glutaminolysis, and fatty acid oxidation.[3] This redox interconversion regulates dehydrogenase activities in catabolic pathways, making real-time monitoring of NAD^+/NADH dynamics a powerful tool to assess cellular energy status, redox homeostasis, and signaling pathway perturbations. Such insights hold significant promise for advancing drug discovery and precision medicine approaches.

Glucose-6-phosphate dehydrogenase (G-6-PD), a critical enzyme in the pentose phosphate pathway,[39] plays a vital role in maintaining redox balance in human erythrocytes. Genetic G-6-PD deficiency represents one of the most prevalent hereditary hemolytic disorders,[40] contributing to neonatal jaundice[41] and acute hemolytic anemia.[40] Quantifying G-6-PD activity enables clinical diagnosis of hemolytic conditions, neonatal screening, safe medication guidance, and genetic counseling.[42,43]

To investigate the function of G-6-PD, a nanopore assay harnessing the discriminative capabilities of MspA-90PBA for NAD^+ and NADH was employed. The enzyme catalyzes the oxidation of glucose-6-phosphate to 6-phosphogluconolactone, concomitantly reducing NAD^+ to NADH.[44,45] The conformational transition from NAD^+ to NADH has been widely reported.[2] Structurally, they exhibit chemical similarity, with the key distinction being that the nicotinamide ring of NAD^+ contains a positively charged quaternary ammonium salt moiety, whereas the corresponding moiety in NADH binds a hydride ion. The redox reaction between NAD^+ and NADH represents a core mechanism in electron transport and ATP production during cellular energy metabolism. $NADP^+$ is biosynthesized from NAD^+ via a

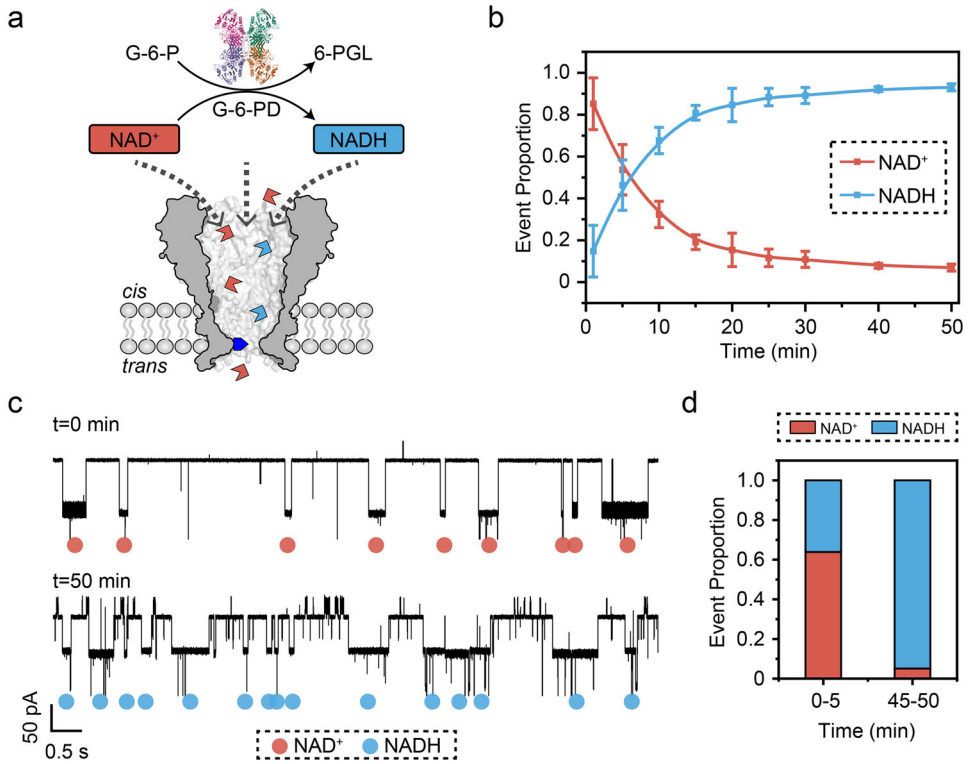

Figure 4. Nanopore monitoring of glucose-6-phosphate dehydrogenase catalysis. a) The schematic diagram of the dehydrogenase catalytic reaction monitored by nanopore. Glucose-6-phosphate dehydrogenase (G-6-PD) can catalyze the conversion of glucose-6-phosphate to 6-phosphogluconolactone (6-PGL), and simultaneously NAD^+ is reduced to NADH. This process can be monitored via the changes of the event proportions of NAD^+ and NADH. b) The event proportion variations of NAD^+ and NADH events during the enzymatic catalysis process. To initiate the measurements, 10 U G-6-PD, 1 mM $MgCl_2$, 5 mM glucose-6-phosphate (G-6-P) and 2 mM NAD^+ were simultaneously added to the *cis* chamber. A potential of +160 mV was continuously applied. The entire enzymatic catalysis process of G-6-PD was monitored and recorded in real time. All nanopore events were identified by the previously trained model. According to different time intervals, the proportions of nanopore events of NAD^+ and NADH were respectively counted, and corresponding curves were plotted. The transformation process of NAD^+ and NADH can be observed via the corresponding proportions of events, thereby enabling real-time monitoring of the enzymatic catalysis process. The statistical results were derived from results of three independent measurements for each condition (N = 3). c) The representative traces acquired at the beginning and 50 min after the initiation of the catalytic reaction. d) The event proportion of NAD^+ and NADH events from 0 to 5 min and from 45 to 50 min respectively. At the beginning of the catalysis, only NAD^+ events were observed. 50 min later, all NAD^+ was exhausted, reporting only NADH events.

kinase-catalyzed phosphorylation reaction. As previously reported,[8] the redox reaction from $NADP^+$ to NADPH is also a critical pathway for electron transport in cellular systems. Both NAD^+[46] and $NADP^+$[47] function as coenzymes for G-6-PD, facilitating its catalytic activity. Here, the conversions of NAD^+ to NADH and $NADP^+$ to NADPH can be monitored via the catalytic activity of G-6-PD. Experimentally, G-6-PD and $MgCl_2$ were added to the *cis* chamber. NAD^+ and the enzyme substrate glucose-6-phosphate were subsequently added to the *cis* chamber to initiate the enzymatic reaction. Nanopore measurements were then continually recorded to monitor the results of the enzymatic reaction in real time (**Figure** 4a,b).

Event classification using a pre-trained machine learning model enabled real-time tracking of NAD^+ and NADH dynamics (Figure 4a–d). At t = 0, only NAD^+ signatures were detected (Figure 4c). As the reaction progressed, NADH events emerged, reflecting the time-dependent conversion of NAD^+ to NADH (Figure 4d). Representative traces obtained at different time points during the dehydrogenase catalysis are shown in Figure S15 (Supporting Information), clearly demonstrating the transition between NAD^+ and NADH. The kinetic profile revealed rapid initial turnover (first 20 min) followed by a decelerating phase approaching equilibrium. Control experiments were also performed, demonstrating that no conversion occurred without NAD^+ (Figure S16, Supporting Information) or substrate (Figure S17, Supporting Information).

Given that both NAD^+ and $NADP^+$ serve as coenzymes for G-6-PD, we performed catalytic measurements of G-6-PD in the simultaneous presence of both coenzymes (**Figure 5**). The entire enzymatic catalysis process, including the transitions between NAD^+/NADH and $NADP^+$/NADPH, was monitored by quantifying the event proportions of NAD^+, NADH, $NADP^+$, and NADPH at distinct time intervals. Notably, G-6-PD displayed a distinctly stronger substrate preference for $NADP^+$ when both coenzymes were present. In the concurrent presence of NAD^+ and $NADP^+$, the nanopore sensor could also detect events of relevant compounds and measure substrate conversion catalyzed by G-6-PD. Although the high concentration of KCl in the measuring buffer used in this work may affect the activity of G-6-PD, numerous experiments have confirmed that G-6-PD still

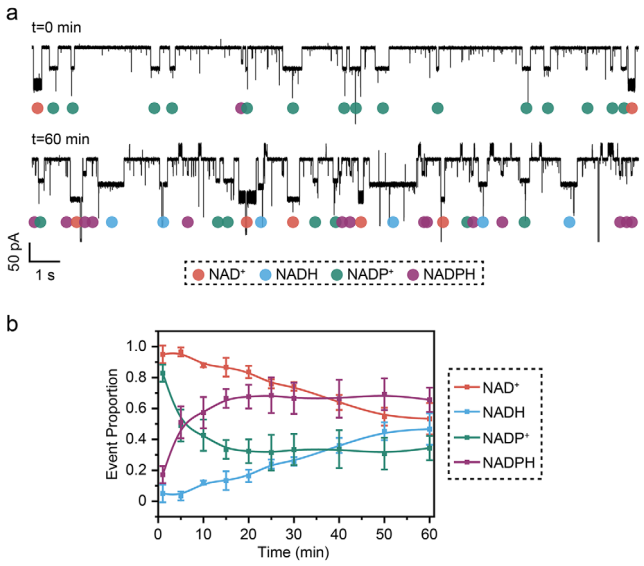

Figure 5. Nanopore monitoring of glucose-6-phosphate dehydrogenase catalysis in the simultaneous presence of NAD^+ and $NADP^+$. Both NAD^+ and $NADP^+$ act as substrates for glucose-6-phosphate dehydrogenase (G-6-PD), which catalyses their conversion to NADH and NADPH, respectively. This process was monitored via changes in the proportions of nanopore events corresponding to NAD^+, NADH, $NADP^+$, and NADPH. For the measurements, 10 U G-6-PD, 1 mM $MgCl_2$, 5 mM glucose-6-phosphate (G-6-P), 1 mM NAD^+, and 1 mM $NADP^+$ were simultaneously added to the *cis* chamber under a continuous +160 mV potential. a) Representative traces at the start and 60 min after initiating the catalytic reaction. Nanopore events for NAD^+, NADH, $NADP^+$, and NADPH were identified and labelled using a pre-trained model. b) Temporal changes in the proportions of NAD^+, NADH, $NADP^+$, and NADPH events during catalysis. Event labels were assigned by the prediction results of the pre-trained model. The entire enzymatic process was monitored in real time, with event proportions quantified at discrete time points. G-6-PD exhibited a kinetic preference for $NADP^+$, as evidenced by the rapid initial turnover of $NADP^+$/NADPH within the first 15 min, followed by a deceleration toward equilibrium. In contrast, NAD^+/NADH required 50 min to reach equilibrium. Statistical results are based on three independent replicates (N = 3), with error bars representing standard deviations.

exhibits catalytic activity under the current measurement conditions. The evaluation of the impact of high-salt environments on enzyme activity would be carried out in the follow-up works. These results validate the use of MspA-90PBA nanopores for monitoring dehydrogenase-catalyzed redox reactions, establishing a novel platform for enzyme activity analysis and inhibitor screening.

3. Conclusion

In summary, the MspA-90PBA nanopore sensor has been successfully demonstrated for multiplex detection of NAD^+ and its derivatives. Eight core analytes, including NAD^+, NADH, $NADP^+$, NADPH, NAMN, NAAD, NMN, and NR, were unambiguously discriminated based on their distinct ionic current signatures during nanopore sensing. Leveraging these unique event features, a tailored machine learning algorithm was developed, which achieved an impressive 99.9% classification accuracy. It enabled real-time analysis of complex mixtures of NAD^+ and its derivatives, providing a high-precision platform for multicomponent analysis without cross-interference. Notably, this label-free methodology eliminates the need for sample amplification or chemical modification, ensuring minimal perturbation to the native states of the sample. The nanopore sensor was also used to analyze yeast extracts, successfully identifying components of NAD^+, NADH and NADPH, highlighting its preliminary applicability in the analysis of complex biological matrices. The utility of this platform was further extended to real time monitoring of glucose-6-phosphate dehydrogenase enzymatic activity. Dynamic changes in NAD^+/NADH and $NADP^+$/NADPH ratios were tracked during catalysis, yielding kinetic insights into redox transformations. These proof-of-concept demonstrations establish a sensing assay for dehydrogenase activity profiling, which holds significant promise for point-of-care diagnostics and metabolic pathway studies in disease contexts.

Supporting Information

Supporting Information is available from the Wiley Online Library or from the author.

Acknowledgements

This project was funded by the National Key R&D Program of China (Grant No. 2022YFA1304602), National Natural Science Foundation of China (Grant No. 22225405), the Fundamental Research Funds for the Central Universities (Grant No. 020514380336), State Key Laboratory of Analytical Chemistry for Life Science (Grant No. 5431ZZXM2509), National Natural Science Foundation of China (Grant No. 22404077, to W.D.J.), the China Postdoctoral Science Foundation (Grant Nos. 2022M721554 and 2023T160300, to W.D.J.), and Jiangsu Funding Program for Excellent Postdoctoral Talent (Grant No. 2023ZB643, to W.D.J.).

Conflict of Interest

S.H. has filed patents describing the preparation of heterogeneous MspA and its applications thereof. The remaining authors declare no other competing interests.

Author Contributions

S.H. and W.D.J. conceived the project. W.D.J. performed the measurements and designed the machine learning algorithms. W.D.J. and L.Y. designed and carried out nanopore measurements of yeast extracts. J.L.C. prepared the MspA nanopores. P.K.Z. set up the instruments. S.H. and W.D.J. wrote the paper. S.H. supervised the project.

Data and Availability Statement

The data that support the findings of this study are available from the corresponding author upon reasonable request.

Keywords

enzymatic reaction, Mycobacterium smegmatis porin A, NAD, nanopore, single molecule

Received: April 7, 2025
Revised: May 22, 2025
Published online: June 17, 2025

[1] S. Chowdhry, C. Zanca, U. Rajkumar, T. Koga, Y. Diao, R. Raviram, F. Liu, K. Turner, H. Yang, E. Brunk, J. Bi, F. Furnari, V. Bafna, B. Ren, P. S. Mischel, *Nature* **2019**, *569*, 570.
[2] A. J. Covarrubias, R. Perrone, A. Grozio, E. Verdin, *Nat. Rev. Mol. Cell Biol.* **2021**, *22*, 119.
[3] S. Amjad, S. Nisar, A. A. Bhat, A. B. R. Shah, M. P. Frenneaux, K. Fakhro, M. Haris, R. Reddy, Z. Patay, J. Baur, P. Bagga, *Mol. Metab.* **2021**, *49*, 101195.
[4] M. E. Migaud, M. Ziegler, J. A. Baur, *Nat. Rev. Mol. Cell Biol.* **2024**, *25*, 822.
[5] S. Lautrup, D. A. Sinclair, M. P. Mattson, E. F. Fang, *Cell Metab.* **2019**, *30*, 630.
[6] E. Verdin, *Science* **2015**, *350*, 1208.
[7] Q. Lin, W. Zuo, Y. Liu, K. Wu, Q. Liu, *Clin. Chim. Acta* **2021**, *515*, 104.
[8] F. Berger, M. H. Ramıŕez-Hernández, M. Ziegler, *Trends Biochem. Sci.* **2004**, *29*, 111.
[9] M. V. Damgaard, J. T. Treebak, *Sci. Adv.* **2023**, *9*, adi4862.
[10] J. Yoshino, J. A. Baur, S.-I. Imai, *Cell Metab.* **2018**, *27*, 513.
[11] Y. Zhao, K. Wei, F. Kong, X. Gao, K. Xu, B. Tang, *Anal. Chem.* **2019**, *91*, 1368.
[12] P. Sun, H. Zhang, Y. Sun, J. Liu, *Spectrochim. Acta, Part A* **2021**, *245*, 118919.
[13] A. Podder, S. Koo, J. Lee, S. Mun, S. Khatun, H.-G. Kang, S. Bhuniya, J. S. Kim, *Chem. Commun.* **2019**, *55*, 537.
[14] Y. Zhao, Q. Hu, F. Cheng, N. i. Su, A. Wang, Y. Zou, H. Hu, X. Chen, H.-M. Zhou, X. Huang, K. Yang, Q. Zhu, X. Wang, J. Yi, L. Zhu, X. Qian, L. Chen, Y. Tang, J. Loscalzo, Y. i. Yang, *Cell Metab.* **2015**, *21*, 777.
[15] Y. Zou, A. Wang, L. i. Huang, X. Zhu, Q. Hu, Y. Zhang, X. Chen, F. Li, Q. Wang, H. Wang, R. Liu, F. Zuo, T. Li, J. Yao, Y. Qian, M. Shi, X. Yue, W. Chen, Z. Zhang, C. Wang, Y. Zhou, L. Zhu, Z. Ju, J. Loscalzo, Y. Yang, Y. Zhao, *Dev. Cell* **2020**, *53*, 240.
[16] P. Wang, M. Chen, Y. Hou, J. Luan, R. Liu, L. Chen, M. Hu, Q. Yu, *Aging Cell* **2023**, *22*, 13965.
[17] Q. Yu, N. Pourmandi, L. Xue, C. Gondrand, S. Fabritz, D. Bardy, L. Patiny, E. Katsyuba, J. Auwerx, K. Johnsson, *Nat. Metab.* **2019**, *1*, 1219.
[18] S. Chen, K. Shang, X. Gao, X. Wang, *Biosens. Bioelectron.* **2022**, *211*, 114376.
[19] W. Guo, H. Wang, Z. Wang, F. Wu, Y. He, Y. Liu, Y. Deng, T. Bing, L. Qiu, W. Tan, *Biosens. Bioelectron.* **2025**, *271*, 116996.
[20] F. S. Omar, N. Duraisamy, K. Ramesh, S. Ramesh, *Biosens. Bioelectron.* **2016**, *79*, 763.
[21] N. Braidy, M. D. Villalva, R. Grant, *Life* **2021**, *11*, 512.
[22] Y.-L. Ying, Z.-L. Hu, S. Zhang, Y. Qing, A. Fragasso, G. Maglia, A. Meller, H. Bayley, C. Dekker, Y.-T. Long, *Nat. Nanotechnol.* **2022**, *17*, 1136.
[23] K. Wang, S. Zhang, X. Zhou, X. Yang, X. Li, Y. Wang, P. Fan, Y. Xiao, W. Sun, P. Zhang, W. Li, S. Huang, *Nat. Methods* **2024**, *21*, 92.
[24] Y. Zhang, Y. Yi, Z. Li, K. Zhou, L. Liu, H.-C. Wu, *Nat. Methods* **2024**, *21*, 102.
[25] M. Zhang, C. Tang, Z. Wang, S. Chen, D. Zhang, K. Li, K. Sun, C. Zhao, Y. Wang, M. Xu, L. Dai, G. Lu, H. Shi, H. Ren, L. Chen, J. Geng, *Nat. Methods* **2024**, *21*, 609.
[26] S. Yan, J. Zhang, Y. Wang, W. Guo, S. Zhang, Y. Liu, J. Cao, Y. Wang, L. Wang, F. Ma, P. Zhang, H.-Y. Chen, S. Huang, *Nano Lett.* **2021**, *21*, 6703.
[27] H. Brinkerhoff, A. S. W. Kang, J. Liu, A. Aksimentiev, C. Dekker, *Science* **2021**, *374*, 1509.
[28] Y. Liu, T. Pan, K. Wang, Y. Wang, S. Yan, L. Wang, S. Zhang, X. Du, W. Jia, P. Zhang, H.-Y. Chen, S. Huang, *Angew. Chem., Int. Ed.* **2021**, *60*, 23863.
[29] N. S. Galenkamp, S. Zernia, Y. B. Van Oppen, M. van den Noort, A. M. Argeitis, G. Maglia, *Nat. Commun.* **2024**, *15*, 10109.
[30] K. Motone, D. Kontogiorgos-Heintz, J. Wee, K. Kurihara, S. Yang, G. Roote, O. E. Fox, Y. Fang, M. Queen, M. Tolhurst, N. Cardozo, M. Jain, J. Nivala, *Nature* **2024**, *633*, 662.
[31] E. A. Manrao, I. M. Derrington, A. H. Laszlo, K. W. Langford, M. K. Hopper, N. Gillgren, M. Pavlenok, M. Niederweis, J. H. Gundlach, *Nat. Biotechnol.* **2012**, *30*, 349.
[32] S. Zhang, Z. Cao, P. Fan, Y. Wang, W. Jia, L. Wang, K. Wang, Y. Liu, X. Du, C. Hu, P. Zhang, H.-Y. Chen, S. Huang, *Angew. Chem., Int. Ed.* **2022**, *61*, 202203769.
[33] S. Zhang, Z. Cao, P. Fan, W. Sun, Y. Xiao, P. Zhang, Y. Wang, S. Huang, *Angew. Chem., Int. Ed.* **2024**, *63*, 202316766.
[34] Y. Liu, S. Zhang, Y. Wang, L. Wang, Z. Cao, W. Sun, P. Fan, P. Zhang, H.-Y. Chen, S. Huang, *J. Am. Chem. Soc.* **2022**, *144*, 13717.
[35] Y. Wang, P. Fan, S. Zhang, L. Wang, X. Li, W. Jia, Y. Liu, K. Wang, X. Du, P. Zhang, S. Huang, *ACS Nano* **2022**, *16*, 21356.
[36] Y. Wang, S. Zhang, W. Jia, P. Fan, L. Wang, X. Li, J. Chen, Z. Cao, X. Du, Y. Liu, K. Wang, C. Hu, J. Zhang, J. Hu, P. Zhang, H.-Y. Chen, S. Huang, *Nat. Nanotechnol.* **2022**, *17*, 976.
[37] A. R. Martin, J.-J. Vasseur, M. Smietana, *Chem. Soc. Rev.* **2013**, *42*, 5684.
[38] X. Liu, W. Feng, F. Yao, J. Zhang, R. Ayesha, T. Chen, X. Shi, X. Qiao, L. Ma, S. Yu, X.-F. Kang, *Anal. Chem.* **2021**, *93*, 7118.
[39] T. TeSlaa, M. Ralser, J. Fan, J. D. Rabinowitz, *Nat. Metab.* **2023**, *5*, 1275.
[40] L. Luzzatto, M. Ally, R. Notaro, *Blood* **2020**, *136*, 1225.
[41] N. Raafat, W. A. Emam, A. F. Gharib, O. E. Nafea, M. Zakaria, *Mycotoxin Res.* **2021**, *37*, 109.
[42] M. Kaplan, C. Hammerman, *Semin. Perinatol.* **2011**, *35*, 155.
[43] H. Y. Lee, A. Ithnin, R. Z. Azma, A. Othman, A. Salvador, F. C. Cheah, *Front. Pediatr.* **2022**, *10*, 875877.
[44] Y. Cui, J. P. Barford, R. Renneberg, *Sens. Actuators, B* **2008**, *132*, 1.
[45] J. S. M Campo, R. Patiño, *Thermochim. Acta* **2011**, *517*, 40.
[46] C. E. Naylor, S. Gover, A. K. Basak, M. S. Cosgrove, H. R. Levy, M. J. Adams, *Acta Crystallogr. Sect. D* **2001**, *57*, 635.
[47] M. Kotaka, S. Gover, L. Vandeputte-Rutten, S. W. N. Au, V. M. S. Lam, M. J. Adams, *Acta Crystallogr. Sect. D* **2005**, *61*, 495.